Nanoscale Vibrational Analysis of Single-Walled Carbon Nanotubes

Neil Anderson,[†] Achim Hartschuh,[‡] Steve Cronin,[§] and Lukas Novotny*,[†]

Contribution from the The Institute of Optics, University of Rochester, Rochester, New York 14627, Physikalische Chemie, Universitat Siegen, 57068 Siegen, Germany, and Department of Physics, Harvard University, Cambridge, Massachusetts 02138

Received August 9, 2004; E-mail: novotny@optics.rochester.edu

Abstract: We use near-field Raman imaging and spectroscopy to study localized vibrational modes along individual, single-walled carbon nanotubes (SWNTs) with a spatial resolution of 10−20 nm. Our approach relies on the enhanced field near a laser-irradiated gold tip which acts as the Raman excitation source. We find that for arc-discharge SWNTs, both the radial breathing mode (RBM) and intermediate frequency mode (IFM) are highly localized. We attribute such localization to local changes in the tube structure (n, m). In comparison, we observe no such localization of the Raman active modes in SWNTs grown by chemical vapor deposition (CVD). The direct comparison between arc-discharge and CVD-grown tubes allows us to rule out any artifacts induced by the supporting substrate.

Introduction

Since their discovery in the early 1990s by Iijima,[1] carbon nanotubes have become the focus of intense interest by many scientists and engineers. The main reason behind such wide-ranging attention lies in their unique electrical,[2] mechanical,[3] thermal,[3] and optical properties.[4] Furthermore, from their size and structure, carbon nanotubes provide a unique system for investigating one-dimensional quantum behavior.[5]

Although many detailed studies have focused on the electronic and mechanical properties of bundles and individual SWNTs, there has, to date, been no extensive spectral analysis of the properties of SWNTs via their vibrational spectrum on the single-tube level with a spatial resolution on the order of 15 nm. Spectral analysis of individual SWNTs has been carried out in the past,[6] but the techniques used were limited by the inability of conventional confocal techniques to image and localize nanoscale features with subwavelength resolution.[7−9] Consequently, localized features, such as defects, could not be resolved so far using optical techniques. In our work, we perform high-resolution optical and atomic force microscopy on individual SWNTs to avoid averaging along the tube length.[10]

Raman spectroscopy is a powerful tool for studying the chemical composition of matter since it yields information about both the electronic and vibrational structure. In this study, we focus on the four main features of SWNT Raman scattering: the radial breathing mode (RBM) [∼100−300 cm^{-1}], the Raman active D band [∼1300 cm^{-1}], G band [∼1592 cm^{-1}], and G′ band [∼2600 cm^{-1}].[11−14] The Raman spectrum provides a unique chemical fingerprint from which to extract a wealth of information on the electronic structure of SWNTs. For example, the tube diameter, chirality, and structure (n, m) [(n, m) defines the atomic coordinates for the 1D unit cell of the nanotube] are associated with the frequency of the RBM; metallic and semiconducting nanotubes can be distinguished based on the shape of the G band (and RBM frequency), and the D band intensity is representative for defects and other disorder-induced effects.

The motivation of this study is to probe, with nanoscale resolution, vibrational modes of spatially isolated, individual SWNTs and to relate spectral variations to changes in the tube structure (n, m) along the tube axis. The ability to go beyond the limits of diffraction-limited spectroscopic techniques is the main advantage of our technique. By introducing a sharp metal probe (tip-enhanced Raman spectroscopy,[10,15−17]) in the focus

[†] University of Rochester.
[‡] Universitat Siegen.
[§] Harvard University.

(1) Iijima, S. et al. *Nature* **1991**, *384*, 56.
(2) Woodside, M. T.; McEuen, P. L. *Science* **2002**, *296*, 1098.
(3) Dresselhaus, M. S.; Dresselhaus, G.; Avouris, P. *Carbon Nanotubes: Synthesis, Structure, Properties and Applications*; Springer-Verlag: New York, 1996.
(4) Hartschuh, A.; Hermeneglido, N. P.; Novotny, L.; Krauss, T. D. *Science* **2003**, *301*, 1354.
(5) Venema, L. C.; Wilder, J. W. G.; Janssen, J. W.; Tans, S. J.; Temminck Tuinstra, H. L. J.; Kouwenhoven, L. P.; Dekker, C. *Science* **1999**, *283*, 52.
(6) Mews, A.; Koberling, F.; Basche, T.; Philipp, G.; Duesberg, G. S.; Roth, S.; Burghead, M. *Adv. Mater.* **2000**, *12*, 1210.
(7) Souza, M.; Jorio, A.; Fantini, C.; Neves, B. R. A.; Pimenta, M. A.; Saito, R.; Ismach, A.; Joselevich, E.; Brar, V. W.; Samsonidze, Ge. G.; Dresselhaus, G.; Dresselhaus, M. S. *Phys. Rev. B* **2004**, *69*, 241403.
(8) McGuire, K.; Gothard, N.; Gai, P. L.; Dresselhaus, M. S.; Sumanasekera, G.; Rao, A. M. *Phys. Rev. B*. Submitted.
(9) Cronin, S. B.; Swan, A. K.; Ünlü, M. S.; Goldberg, B. B.; Dresselhaus, M. S.; Tinkham, M. *Phys. Rev. Lett.* **2004**, *93*, 167401.

(10) Hartschuh, A.; Sanchez, E. J.; Xie, X. S.; Novotny, L. *Phys. Rev. Lett.* **2003**, *90*, 095503.
(11) Jorio, A.; Saito, R.; Hafner, J. H.; Lieber, C. M.; Hunter, M.; McClure, T.; Dresselhaus, G.; Dresselhaus, M. S. *Phys. Rev. Lett.* **2001**, *86*, 1118.
(12) Reich, S.; Thomsen, C.; Maultzsch, J. *Carbon Nanotubes: Basic Concepts and Physical Properties*; Wiley-VCH: Weinheim, Germany, 2004.
(13) Rao, A. M.; Richter, E.; Bandow, S.; Chase, B.; Eklund, P. C.; Williams, K. A.; Fang, S.; Subbaswamy, K. R.; Menon, M.; Thess, A.; Smalley, R. E.; Dresselhaus, G.; Dresselhaus, M. S. *Science* **1997**, *275*, 187−191.
(14) Bachilo, S. M.; Strano, M. S.; Kittrell, C.; Hauge, R. H.; Smalley, R. E.; Weisman, R. B. *Science* **2002**, *298*, 2361.
(15) Wessel, J. *J. Opt. Soc. Am. B* **1985**, *2*, 1538−1540.
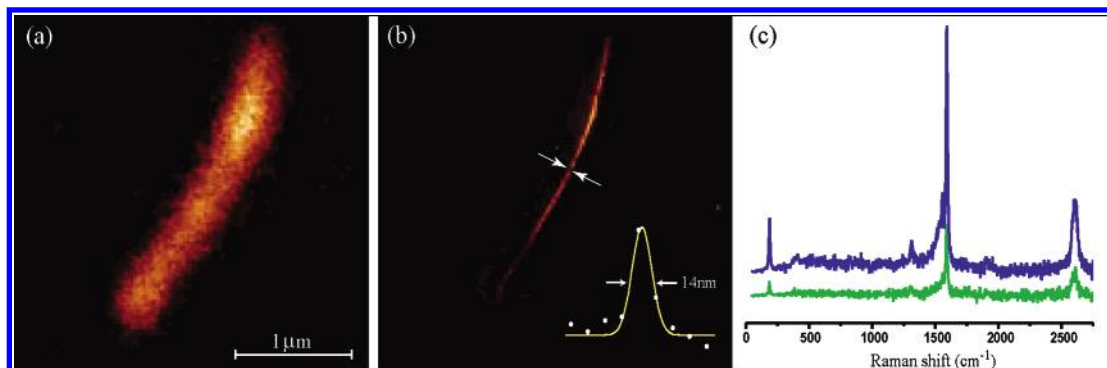
Figure 1. (a and b) Raman scattering images of a single SWNT deposited on a glass coverslip. The contrast in the images reflects the local intensity of the Raman G′ band (2640 cm^{-1}). (a) Confocal Raman image (fwhm of 275 nm); and (b) the corresponding near-field Raman image. The integration time was 10 ms per image. The inset in (b) shows a Gaussian fit to the line section shown (fwhm of 14 nm). (c) Raman scattering spectrum for a single SWNT with (blue) and without (green) a metal tip present. No changes in the peak positions for the Raman bands shown were recorded in the presence of the metal tip. The graphs are offset for clarity.

of a laser beam, we are able to localize the Raman excitation area to ∼15 × 15 nm^2. The high spatial frequencies associated with this electromagnetic field confinement allow us to record (near-field) Raman images of SWNTs with a spatial resolution on the order of 10−20 nm. Spectroscopic information can then be extracted locally as we position our probe along a SWNT of interest. In this way, we are able to acquire simultaneously vibrational maps that show the evolution and variation of several Raman active modes and corresponding topographic profiles along many different SWNTs. We believe that the ability to map spectral changes along SWNTs, with nanoscale precision, will lead to a greater understanding of the fundamental properties of such materials on the single-tube level.

Experimental Section

Our near-field Raman setup[10] is based on an inverted optical microscope with the addition of an *x, y* stage for raster-scanning samples. Light from a He−Ne laser (633 nm, 50−200 μW) is reflected by means of a dichroic beam splitter and then focused onto the surface of the sample using a high numerical aperture objective (N.A. = 1.4).

Having obtained a tight focal spot at the sample surface, we then position a sharp metal tip into the focal region. We carefully align the tip with one of the two longitudinal field components in the focal plane.[18] The metal tip is held at a constant height of 2 nm by means of a shear-force detection feedback mechanism[19] with an RMS noise of ∼0.5 Å in the *z*-direction. Using the *x, y* scan stage to raster scan the sample, Raman scattered light is collected by the same microscope objective and recorded using either a single-photon counting avalanche photodiode (APD) or a spectrograph with a charged-coupled device (CCD) cooled to −124 °C. Typical acquisition times for recording a full Raman spectrum that is assigned to a particular image pixel (*x, y*) is on the order of 100 ms.

SWNTs were produced by two distinct processes, namely, by arc-discharge and chemical vapor deposition (CVD).[3] The arc-discharge SWNTs were dispersed in a solution of dichloroethane, sonicated in an ultrasonic bath, and spin cast at 3000 rpm onto a glass coverslip. CVD-grown SWNTs were produced on a supporting quartz substrate using a iron (III) nitrate catalyst at a temperature of 800 °C. Gold tips were produced by electrochemical etching of thin gold wire in a solution of hydrochloric acid (HCl) for ∼30 s.

(16) Hayazawa, N.; Inouye, Y.; Sekkat, Z.; Kawata, S. *Chem. Phys. Lett.* **2001**, *335*, 369−374.
(17) Stockle, S. M.; Suh, Y. D.; Deckert, V.; Zenobi, R. *Chem. Phys. Lett.* **2000**, *318*, 131−136.
(18) Novotny, L.; Sanchez, E. J.; Xie, X. S. *Ultramicroscopy* **1998**, *71*, 21.
(19) Karrai, K.; Grober, R. D. *Appl. Phys. Lett.* **1995**, *66*, 1842.

Results

The ability to perform high-resolution microscopy is demonstrated in Figure 1. Figure 1a shows a diffraction-limited confocal Raman image recorded by raster-scanning a sample with a single SWNT through the focused laser. The contrast in the image results from integrating the Raman spectrum for each image pixel over a narrow spectral range centered at $\nu = 2600$ cm^{-1} (G′ band). Figure 1b shows the corresponding near-field Raman image taken over the exact same sample area and results from placing a sharp metal tip into the laser focus. The spatial resolution is ∼14 nm (fwhm), as shown by the inset of Figure 1b. Representative Raman spectra with and without the tip present are shown in Figure 1c. The increase in Raman scattering strength clearly demonstrates the effect of surface-enhanced Raman scattering (SERS). The Raman enhancement factor depends on the ratio of the near-field and confocal interaction volumes. Typical enhancement factors are in the range 10^2-10^4.[10]

We study the spatial dependence of the four main Raman active bands for an individual SWNT grown by the arc-discharge method. Figure 2a−d shows a series of near-field spectral images of two individual SWNTs corresponding to the G, G′, D, and RBM Raman active modes, respectively. From these images, one can clearly observe the spatial variation in Raman scattered light for all four Raman bands. Both the G and G′ bands show a near-uniform intensity profile along the nanotube in the center of the image. A similar uniform distribution is observed for the weak disorder-induced D band (see Figure 2c). However, the most striking spectral feature is the localized scattering associated with the RBM of the nanotube studied. Figure 2d shows that the RBM is only detected in the center region of one of the nanotubes, namely, the SWNT in the center of the image. The other SWNT is not resonantly excited with our excitation source. The detected radial mode frequency of the first SWNT was measured to be ∼205 cm^{-1}, indicating that we observe a (14, 1) nanotube. Using the relation $\nu_{RBM} = A/d_t + B$ (where $A = 223.5$ nm/cm and $B = 12.5$ cm^{-1}),[14] we calculate the nanotube diameter to be 1.16 ± 0.2 nm. Simultaneous AFM measurements confirm that it is indeed a single SWNT, its diameter being measured topographically as 1.2 ± 0.3 nm (see Figure 2e).

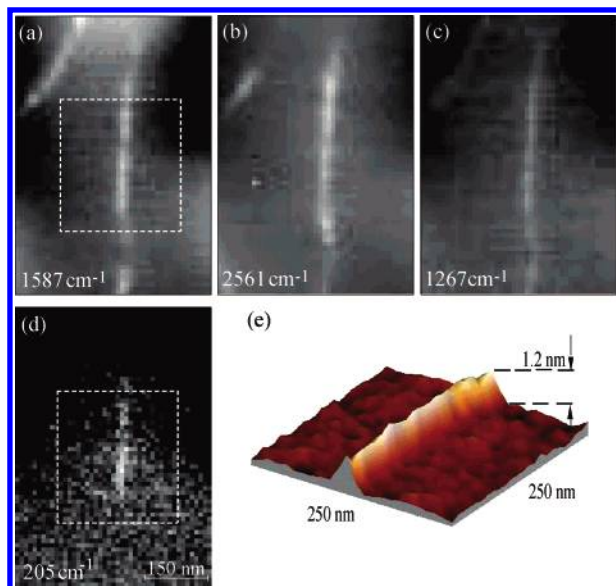To understand the origin of these local variations, we first discuss the resonance conditions associated with the different

Figure 2. Near-field spectral images, upon laser excitation at 633 nm, for the Raman active G band (a), G′ band (b), D band (c), and RBM (d). (e) A 3D topographical profile (cf. dashed box). The images were produced from the Raman scattered light detected with a cooled CCD. The integration time was 210 ms per image pixel. The most striking feature is the localization of the RBM associated with the vertically aligned SWNT. From the measured RBM frequency of 205 cm^{-1}, we assign a tube structure of (14, 1).

Figure 3. Near-field spectral images for the Raman active G band (a), RBM (b), and intermediate frequency mode (IFM), centered at 765 cm^{-1}. Integration time of 210 ms per image pixel. (d) The 3D profile taken from the simultaneously acquired topographical image. The attached particles, ∼3 nm in height, are presumably enclosed Ni/Y catalyst particles left over from the growth process. From the measured RBM frequency of 143 cm^{-1}, we assign a tube structure of (20, 3). The asterisks indicate the location of the start and end of the SWNT imaged.
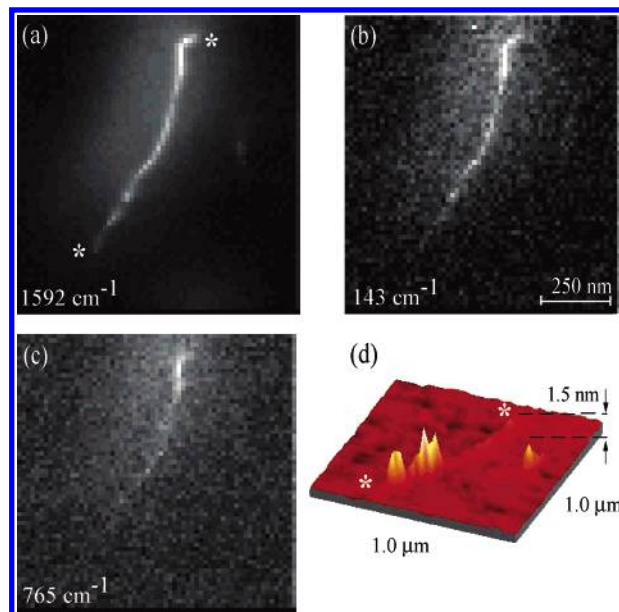
Raman bands. Compared to that of the G, G′, and D bands, the RBM has a sharp resonance window.[7] The RBM is more likely to change in the presence of tube defects, such as localized changes in the structure of the tube lattice [changes in (n, m)], kinks, and intertube junctions in addition to interactions with the glass substrate on which the tubes are dispersed. Any of these variations will affect the van Hove transition energy, E_{ii}, and detune the RBM out of resonance and, thus, lead to a lowering or disappearance of the RBM line. For the G, G′, and D Raman active bands, any small change in E_{ii} is unlikely to manifest itself in similarly dramatic spectral variations along the length of a single nanotube.

Figure 2c reveals the presence of scattered light associated with the Raman D band centered around 1267 cm^{-1}. In light of the weak signal associated with this band, we relate such scattering to disorder-induced effects within the nanotube lattice itself or the coupling to the supporting substrate. In a related study on boron-doped SWNTs,[20] we observed significant intensity increases and localization of D band Raman scattering along several different SWNTs in addition to observing similar variations for both the G and G′ bands.[21]

We like to emphasize that the variations in the spectral images (Figure 2) are not an artifact induced by the presence of the metal tip, that is, by variations in the tip−sample distance. Any such effect on the local Raman spectrum would manifest itself in large height variations in the simultaneously recorded topographic map. The latter is shown in Figure 2e for the nanotube studied (cf. dashed boxes). It is evident that we observe only small tip−sample height variations, on the order of 0.1− 0.2 nm, as the sample is raster-scanned. We, therefore, conclude

that the origins of the localized RBM scattering lie in variations within the tube structure (n, m) and are not related to variations in tip−sample separation.

Our observation and explanation of the RBM localization is consistent with the results that we acquired for many different SWNT structures (assigned from RBM frequency). In Figure 3a−e, we show further evidence for localized Raman scattering associated with the following Raman active modes, namely, the G band (a), RBM (b), and intermediate frequency mode (IFM) (c).[13] Figure 3d shows a simultaneously recorded AFM profile of the nanotube studied. Once again, we observe localized spectral variations of the RBM for a (20, 3) SWNT. The RBM signal decreases significantly in the presence of 3 nm high particles (presumed to be enclosed Ni/Y catalyst particles) located at the nanotube end. This observation is consistent with the idea that changes in the nanotube structure can lead to a loss of resonance Raman scattering properties of SWNTs.

Over the same section of nanotube, we observe a near-uniform spatial variation of the G band (see Figure 3a). The same observation holds for the G′ band (data not shown). However, Raman scattering associated with the RBM is present at only spatially distinct sections along the nanotube. Therefore, we conclude that the spatial variations observed are a manifestation of defects in the nanotube structure or a direct result of the nanotube purification and separation processes, in addition to nanotube−substrate coupling. The fact that the G band is relatively unaffected by the attached particles indicates that the nanotube itself remains intact for ∼250 nm beyond the point of the last (catalyst) particle attached to the nanotube surface.

The vibrational mode shown in Figure 3c is recorded along a single SWNT for the first time. The band is designated as an intermediate frequency mode (IFM) and is known from the literature.[13] To the best of our knowledge, there has been no

(20) Maultzsch, J.; Reich, S.; Thomsen, C.; Webster, S.; Czerw, R.; Carroll, D. L.; Vieira, S. M. C.; Birkett, P. R.; Rego, C. A. *Appl. Phys. Lett.* **2002**, *81*, 2647.
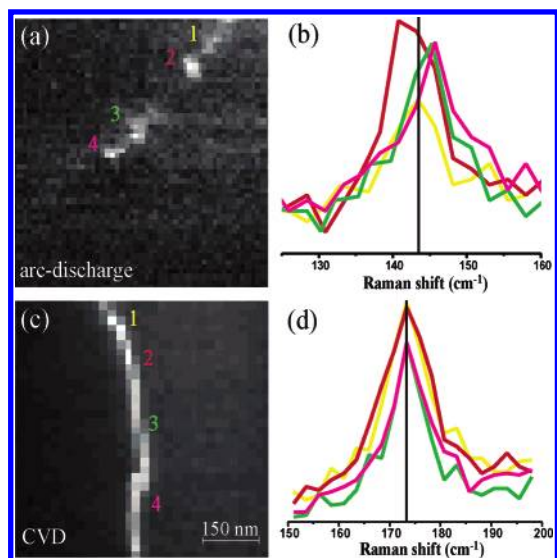(21) Anderson, N.; Hartschuh, A.; Rao, A. M.; Novotny, L. In preparation.

Figure 4. (a and c) Near-field spectral images for the RBM of an arc-discharge-grown SWNT [143 cm^{-1}, (20, 3)] and a SWNT grown via CVD [173 cm^{-1}, (13, 7)], respectively. The integration time was 210 ms per pixel. (b and d) Corresponding RBM spectra for several locations along the length of the SWNTs as marked. The most notable feature is the spectral wandering of the RBM peak for the arc-discharge-grown nanotube and the variation in intensity. In comparison, RBM scattering for the CVD-grown nanotube shows no such spatial variation in intensity and RBM frequency.

previous attempt to understand why the IFM is localized similar to the observed spatial variations of the RBM. We conclude that the IFM is dependent on the nanotube structure (n, m) in a manner similar to that of the RBM. This claim is strengthened by the fact that this band is not always detectable for either SWNT bundles or individual SWNTs using an excitation wavelength of 633 nm. Future work should provide a more detailed insight into the spatial variation of these two bands and any possible dependence on the structure of SWNTs.

To further support our observations, we performed a comparison of arc-discharge-grown SWNTs and SWNTs produced via the CVD growth method. Figure 4 shows the spatial variation of the RBM frequencies for both types of nanotube. Figure 4a reveals that the RBM is not constant along the length of the arc-discharge nanotube and is, in some regions, undetectable. In addition to RBM intensity variations, we also observe spectral wandering, on the order of 2–3 cm^{-1}, of the RBM frequency (cf. Figure 4b). This effect is primarily attributed to structural defects in the nanotube lattice (which may be the result of the sonication process used to separate the SWNTs) that detune the RBM out of resonance.

Figure 4c shows the spatial variation of the RBM along a CVD-grown SWNT. It is evident that the signal is uniform and not localized as in the case of the arc-discharge nanotube. Similar results were obtained for other CVD-grown nanotubes, and the observation of RBM distributions is consistent in all measurements. We conclude that the lack of significant variations of the RBM frequencies for CVD-grown nanotubes indicates that the tube structure [i.e., (n, m)] remains intact, even when the nanotube is resting on a supporting substrate. This claim is further strengthened by the fact that the peak position of the measured RBM frequency also remains constant (see Figure 4d). The most plausible explanation for the observed variations in RBM frequencies of arc-discharge nanotubes and
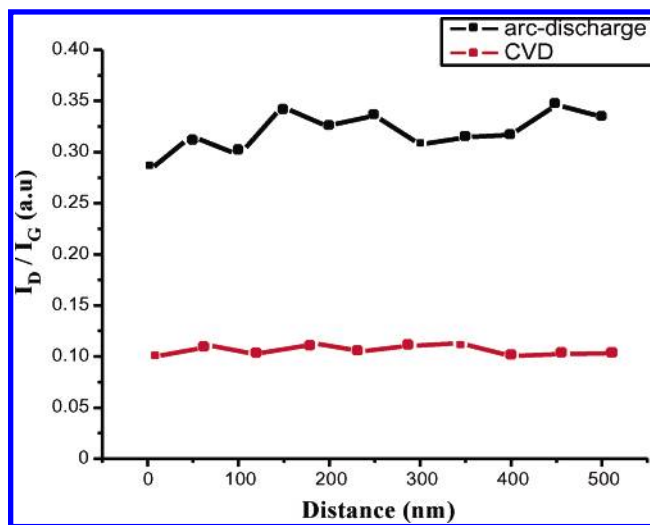
Figure 5. Plot of I_D/I_G versus distance along an arc-discharge and a CVD-grown SWNT. The step size is 50 nm.

the localization thereof is related to defects in the nanotube lattice.

To quantify the defect density in carbon nanotubes, we take the ratio of the D band intensity to the G (or G′) band intensity.[20] Figure 5 shows a plot of I_D/I_G, in increments of 50 nm, along a section of two different SWNTs, an arc-discharge nanotube, and a CVD-grown nanotube. This type of defect mapping reveals a lower value of I_D/I_G for the CVD-grown nanotube compared with that of the nanotube grown by arc-discharge, indicating that there are less disorder-induced effects in CVD nanotubes. However, our technique is limited in that it can only highlight nanotube defects on a length scale of ∼15 nm, and variations on the atomic level are averaged out. To acquire more precise structural information on lattice defects, one would need to perform measurements with scanning tunneling microscopy (STM) or transmission electron microscopy (TEM). On the other hand, STM is only able to map defects in the nanotube that can be accessed with the STM tip, that is, defects underneath the tube remain hidden. Near-field Raman imaging takes an average reading of the local nanotube circumference and, therefore, could be able to access these hidden defects.

We note here that the measured values for the RBM frequencies with and without a metal tip present were identical for the CVD SWNTs studied. However, for the arc-discharge nanotubes, this appears not to be the case since our near-field analysis reveals that the RBM peak position changes for different sections along the nanotube length. Therefore, any confocal measurement must take into account the fact that averaging over several different RBM frequencies may occur.

The same metal tip was used to study all the SWNTs presented in this article. On the basis of calculations, we determined the SERS enhancement factor to be on the order of 10^3.

Conclusion

In conclusion, we have, using near-field Raman imaging and spectroscopy, mapped the vibrational modes along spatially isolated, individual SWNTs with a spatial resolution of ∼15 nm. Our results demonstrate that high-resolution microscopy is necessary to avoid averaging of the Raman spectrum along individual SWNTs. As such, our results reveal the localized

nature of the light scattering associated with the radial breathing mode (RBM) and intermediate frequency modes (IFM) from SWNTs produced by arc-discharge. We attribute these variations to local defects in the nanotube lattice. Spectral analysis of the nanotubes studied reveals that for arc-discharge SWNTs, the RBM peak position changes with spectral shifts on the order of $2-3$ cm^{-1}. We observe no such spectral shifts in measuring the RBM frequency for CVD-grown SWNTs. Furthermore, we have seen little or no significant spatial and spectral variation for both the G and G′ Raman active bands for all SWNTs studied. Finally, we have observed detectable Raman scattering associated with disorder-induced effects. In mapping the I_D/I_G ratio along individual nanotubes, we observe significant varia-tions for SWNTs grown by arc-discharge. In contrast, we observe a much lower value for I_D/I_G on CVD-grown SWNTs, indicating the relatively defect-free nature of such nanotubes.